SENSITIVITY ANALYSIS FOR THE OPTIMIZATION OF RADIOFREQUENCY ABLATION IN THE PRESENCE OF MATERIAL PARAMETER UNCERTAINTY

Inga Altrogge,[1] Tobias Preusser,[2,3] Tim Kröger,[4] Sabrina Haase,[3] Torben Pätz,[2,3] & Robert M. Kirby[5,*]

[1]Center of Complex Systems and Visualization, University of Bremen, Germany.

[2]School of Engineering and Science, Jacobs University Bremen, Germany.

[3]Fraunhofer Institute for Medical Image Computing MEVIS, Bremen, Germany.

[4]Georg Simon Ohm University of Applied Sciences, Nuremberg, Germany.

[5]School of Computing, The University of Utah, Salt Lake City, USA.

We present a sensitivity analysis of the optimization of the probe placement in radiofrequency (RF) ablation which takes the uncertainty associated with bio-physical tissue properties (electrical and thermal conductivity) into account. Our forward simulation of RF ablation is based upon a system of partial differential equations (PDEs) that describe the electric potential of the probe and the steady state of the induced heat. The probe placement is optimized by minimizing a temperature-based objective function such that the volume of destroyed tumor tissue is maximized. The resulting optimality system is solved with a multi-level gradient descent approach. By evaluating the corresponding optimality system for certain realizations of tissue parameters (i.e. at certain, well-chosen points in the stochastic space) the sensitivity of the system can be analyzed with respect to variations in the tissue parameters. For the interpolation in the stochastic space we use a stochastic finite element approach with piecewise multilinear ansatz functions on adaptively refined, hierarchical grids. We underscore the significance of the approach by applying the optimization to CT data obtained from a real RF ablation case.

KEY WORDS: stochastic sensitivity analysis, stochastic partial differential equations, stochastic finite element method, adaptive sparse grid, heat transfer, multiscale modeling, representation of uncertainty.

1. INTRODUCTION

The interstitial thermal destruction of lesions with radiofrequency (RF) ablation has become a widely used technique for the treatment of tumor diseases in various organs. The focus of this work concentrates on the RF ablation of lesions in the liver. In RF ablation, a probe which is connected to an electric generator is placed in the malignant tissue. Upon turning on the generator, the tissue is heated by an electric current due to its Ohm resistance. The heat causes the coagulation of proteins and consequently tissue cells die. The treatment is considered successful if all malignant cells are completely destroyed including a safety margin of about 0.5–1cm; (cf. e.g., [1]).

The success of an RF ablation treatment depends heavily on the anatomical configuration and on the experience of the attending medical doctor. As blood vessels in the vicinity of the lesion transport away the heat which is generated by the electric current, there is the risk that tumor cells close to blood vessels are not destroyed. As a consequence,

---

*Correspond to: Robert M. Kirby, E-mail: kirby@cs.utah.edu, URL: http://www.cs.utah.edu/~kirby

local recurrences may result, and indeed there are recurrence rates of up to 60% reported in the literature [2]. Today it mostly depends on the experience of the attending radiologist, surgeon or gastroenterologist to select the therapy parameters, i.e., the placement of the probe and the settings of the electric generator such that the local blood flow does not hinder the success of the therapy.

These expositions motivate many during the last decade to investigate RF ablation scenarios using mathematical modeling, simulation and optimization. The common goal is to understand the biophysical processes involved in this treatment form and to allow for the planning of an optimal treatment for an individual patient in advance, which would yield the greatest therapy quality and success.

The mathematical/bio-physical models of this scenario which have been developed so far result in systems of partial differential equations (PDEs) [3–6]. These systems allow for a numerical simulation of RF ablation yielding a prediction of the outcome for a given placement of the probe and power of the generator. Clearly, these models depend on the physical properties of the tissue, i.e., their electrical and thermal properties such as electrical and thermal conductivity, heat capacity, density, and water content.

The modeling of these tissue properties poses a particular challenge because they depend on the current state of the tissue, e.g., the electrical conductivity depends on the temperature, the water content, and also on the grade of destruction of the tissue [3, 7, 8]. Moreover, the tissue properties vary inter-individually, and in fact they are not exactly known. Values used in simulations are, for example, often based on *ex-vivo* experiments of animal tissue [3]. In addition, experimental measurements are always accompanied with a certain range of errors. Consequently, truly patient-specific models for RF ablation are not currently feasible, and the question arises whether results obtained through simulations can be used efficaciously in the clinical setting. In our view, the issue of patient specific models and simulations is in fact the most challenging task for mathematical modeling and simulation in medicine.

For practical purposes, more relevant than the simulation of RF ablation, is the inverse problem of finding an optimal placement for the RF probe such that a given lesion is completely destroyed. This optimization problem has been investigated by the authors with thorough mathematical approaches that minimize certain objective functions [9–12]. The role of the objective function is to measure the "quality" of a given probe placement; a quantification of quality provides insight into the deviation of the achieved temperature from a desired temperature. Clearly this involves the use of one of the aforementioned models for forward simulations of RF ablation. In this paper we make first steps toward combining the optimization of the probe placement with the analysis of the uncertainty that is associated with material parameters, i.e., we investigate the sensitivity of the optimal probe placement with respect to variations in the material parameters.

We start with a deterministic model for the electric potential of the RF probe and for the steady state of the temperature distribution. In our approach we do not consider the electric and thermal conductivity to have fixed values, but to be probabilistically distributed. The ranges for these parameters can be taken from experiments which are documented in the literature, or estimations of the measurement error can be taken into account. Substituting the probabilistically distributed values into the PDE-model for the simulation of RF ablation yields a system of stochastic partial differential equations (SPDEs).

There are several different methods to discretize this system. Probably the most popular approach is the (rather slowly converging) Monte Carlo simulation, which is a non-intrusive sampling methodology that requires a large number of randomly chosen sampling points to completely cover the stochastic space. Another well known approach is the stochastic Galerkin method, which uses an approximation of the stochastic process by a finite linear combination of stochastic basis functions. It works with the weak formulation of the SPDE system to obtain an approximate solution. Although the stochastic Galerkin method provides high accuracy and fast convergence, it is not always the best suited (i.e., most computationally efficient) method for solving large problems because of its intrusive nature [13]. To address this problem, combinations of both methods have been developed that work with an approximation representation of the stochastic process and evaluate the resulting weak formulation at carefully chosen (sparse) grid points within the random space to compute accurate statistics with significantly fewer solutions than in the Monte Carlo simulation. One result of such combinations is the stochastic collocation method, which uses polynomial basis functions for the approximation of the stochastic process and thus requires a smoothly-varying dependence of the model on the stochastic input parameters (i.e., on the tissue properties). Another resulting method is a stochastic

finite element approach (also referred to as the collocating multi-element generalized polynomial chaos method) with e.g., piecewise multilinear ansatz functions on adaptively refined, hierarchical grids in the stochastic space. Here we relax the smoothness requirements compared to the stochastic collocation method at the cost of more sampling points in the stochastic space. However, in comparison to Monte Carlo, we still gain in terms of efficiency by requiring fewer solution evaluations while obtaining much better convergence.

By evaluating the SPDE system for certain realizations of the material parameters we can analyze the sensitivity of the system with respect to variations in the coefficients of the PDE system, i.e., with respect to variations in the material parameters. To compute this sensitivity analysis we take a stochastic finite element approach into account using piecewise multilinear ansatz functions for the interpolation in the stochastic space. Moreover, an adaptive grid refinement is performed in critical stochastic regions. The reason for using this approach instead of a stochastic collocation method for analyzing the sensitivity of our optimization are the weaker smoothness requirements mentioned above.

1.1 Related Work

The numerical simulation of RF ablation (and related thermal-therapies) has been considered by many authors [3, 4, 6, 14, 15]. A particular focus has been emphasized concerning the modeling of blood flow and its effect on the temperature distribution during RF ablation [5, 14, 16]. The optimization of the probe placement through a minimization of the L^2 distance between the achieved temperature and a critical temperature inside the tumor has first been considered by the authors in [9]. In [10] we have extended this approach to a non-symmetric penalization, thus allowing for temperatures which are above the critical temperature. Moreover, we generalized the former approach toward probe-clusters and use a hierarchical multi-scale optimization algorithm. A further modification of our optimization that uses shape derivatives instead of central differences for the calculation of the descent direction in order to increase the robustness (i.e., the starting point independency) of our optimization algorithm will be published in [11]. In [17] Villard *et al.* approximate the complicated optimization with PDE constraints by a simple geometric optimization which uses templates for the elliptical shapes of temperature isosurfaces generated by RF probes. Butz *et al.* [18], who focus on the optimization of cryo-therapy, but consider RFA as well, also use ellipsoidal approximations of the ablation zone, which they have obtained from the literature and additional experiments. Moreover, a related form of therapy (interstitial ultrasound) has been optimized in [19]. In [20] Seitel, Villard and Baegert *et al.* present a trajectory planning system for percutaneous insertions that extents the work of Villard and Baegert [1, 21] and determines rated possible insertion zones/trajectories via hard and soft constraints using the concept of pareto optimality. However, here the ablated tissue region and its coverage of the tumor seems not to be under consideration (i.e., part of the soft constraints) any more. Kapoor *et al.* [22] formulate the task of optimizing the number and placement of multiple RF needle probes as mixed variable optimization problem with hard and soft constraints, which they solve with a derivative-free class of algorithms called mixed variable mesh adaptive direct search. In contrast to Seitel, Villard and Baegert *et al.* [20], they take into account the optimal thermal ablation coverage, but again use ellipsoidal shaped approximations of single probe ablation zones, which are then combined to the resulting necrosis. In particular, they do not take into account the cooling effect of large blood vessels close by the tumor. In [23] Chen *et al.* optimize the RF probe's insertion depth and orientation under the assumption of a given, fixed entry point of the probe. They use an objective function that depends on the survival fraction, which is predicted by a finite element computation of the Arrhenius formalism, but which is also approximated as a field that transforms rigidly with the electrode, during the optimization. To the best of our knowledge none of the above approaches considers the uncertainty that is associated with tissue parameters due to their patient- and state dependence, as well as due to measurement errors.

The main stochastic theoretical underpinning of this work is generally referred to as *generalized Polynomial Chaos*. Based upon the Wiener-Hermite polynomial chaos expansion [24], generalized polynomial chaos seeks to approximate second-order random processes by a finite linear combination of stochastic basis functions. Once one has chosen an approximation space of the random process of interest, a solution within that space can be found by solving the stochastic partial differential system of interest in the weak form. Because of its analogy with the classic Galerkin method as employed in finite elements, this methodology is often referred to as the generalized Polynomial Chaos - Stochastic Galerkin method (gPC-SG). It has been applied as a method for uncertainty quantification in the

field of computational mechanics for a number of years and has recently seen a revival of interest [25–32]. This approach has also been applied successfully within the biological modeling world. In [33], Geneser *et al.* employed the gPC-SG approach to evaluate the effects of variations and uncertainty in the conductivity values assigned to organs in a two-dimensional electrocardiograph simulation of the human thorax.

Although the stochastic Galerkin method provides a solid mathematical framework from which one can do analysis and can derive algorithms, it is not always the most computationally efficient means of solving large problems. Nor is it the case that one always has the freedom to re-architect their currently available deterministic solver to employ gPC-SG. To address these issues, the non-intrusive stochastic collocation (SC) method was developed [34].

For the sensitivity analysis of our optimization with respect to changes in the tissue parameters we use a stochastic (collocating) finite element approach (see e.g., [35, 36]) with piecewise multilinear basis functions, which need weaker smoothness requirements on the stochastic optimality system than global polynomial basis functions as used in the traditional gPC approach. This multi-element approach is often referred to as the "multi-element polynomial chaos method" (MEgPC) [37, 38], which has both Galerkin and Collocation variants and allows the user to decide the level of smoothness that will be exploited in the random space through a combination of both element spacing (in the random space), polynomial order, and smoothness conditions between (stochatic) elements.

The optimization problem considered in this paper lies in the field of nonlinear optimization subject to infinite dimensional constraints given by a system of (stochastic) partial differential equations. For an overview of the methodology we refer the reader to [39]. The consideration of uncertainty in inverse problems and optimization problems with PDE constraints has not yet received much attention in the community. The estimation of parameters in the presence of noisy measurements has been treated with the Bayesian inference approach, which uses known information about the parameters to create a priori distribution [40–42]. A first approach to stochastic inverse problems is presented by Zabaras and Ganapathysubramanian in [43] where the solution of the stochastic inverse heat equation is obtained with the method of polynomial chaos. A stochastic collocation approach to the solution of optimal control problems with stochastic PDE constraints is presented in [44]. In this work the authors derive a gradient descent method as well as a sequential quadratic program for the minimization of objective functions of tracking type, which involve stochastic moments of the state variables.

1.2 Paper Organization

The paper is organized as follows: In Section 2 we briefly review a (deterministic) mathematical model for the simulation of RF ablation and the optimization of the probe placement. We discuss a suitable objective function and a multi-scale gradient descent algorithm for the solution of the optimality system.

In Section 3 we introduce the notion of random fields as a model for the uncertainty associated with material parameters. The extension of the deterministic PDE model to an SPDE system is presented in Section 3.1.

In Section 3.2 we give a short overview of some popular methods for the stochastic discretization and in particular describe the stochastic finite element method as used in this work. Further, in Section 3.3 two different approaches for an analysis of the sensitivity of the optimal probe placement with respect to variations in the material parameters are discussed. Finally, applications are presented in Section 4 and conclusions are drawn in Section 5.

2. OPTIMIZATION OF RF ABLATION

In this section we present a model for the simulation of the RF ablation and for the optimization of the probe placement. We consider the computational domain to be a cuboid $D \subset \mathbb{R}^3$ in the three-dimensional space with boundary $B = \partial D$ in which a tumor $D_t \subset D$ and vascular structures $D_v \subset D$ are located. Furthermore, we assume that a mono-polar RF probe is applied in D, whose position $p \in D$ (of the active zone's center) and direction $a \in S^2 = \{x \in \mathbb{R}^3 : |x| = 1\}$ are variables (over which we would like to optimize later). The subset of D that is covered by the probe is denoted by D_{pr}, and the subset covered by the electrode is denoted by D_{el} (cf. Fig. 1). Note that these sets depend on p and a. In practical applications the sets D_t and D_v are determined from segmented image data in advance, e.g., by the methods presented in [45]. Moreover, to achieve the desired safety margin we can consider D_t to be a dilated version of the original segmented tumor mask.
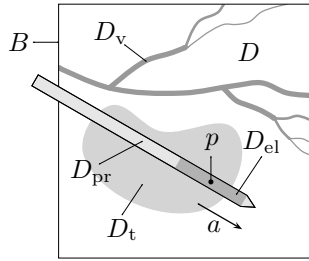
Figure 1: Schematic sketch of the considered configuration identifying the different geometric regions specified in the text. Note that $D_{\text{el}} \subset D_{\text{pr}}$ where both sets depend on p and a.

2.1 Simulation of RF Ablation

Let us now describe how to compute the heat distribution in the tissue D for a fixed position and orientation of the probe, that is, for fixed D_{pr} and D_{el}. The forward simulation model consists of two parts. The first component is the electrostatic equation that describes the electric potential of the tissue which is induced by the electric potential of the electrodes. The second component is the heat equation which models the distribution of temperature once the heat source from the electric potential is known.

The electric potential $\phi : D \to \mathbb{R}$ of the RF probe is modeled by the *electrostatic equation*

$$-\text{div}(\sigma(x)\nabla\phi(x)) = 0 \qquad\qquad \text{in } D \setminus \overline{D_{\text{el}}} \qquad\qquad (1)$$

with appropriate boundary conditions (see below). Here, $\sigma : D \to \mathbb{R}$ is the electric conductivity of the tissue. It is known that the electric conductivity also depends on the temperature, the water content and the protein state of the tissue. More refined models for the forward simulation take this behavior into account [46, 47]. However, since our approach is a first step towards an optimization of the probe placement (i.e., the inverse problem), we do not consider this dependence and just investigate spatial variation of $\sigma = \sigma(x)$.

For the electrostatic equation (1) we consider the inner boundary condition

$$\phi = 1 \qquad\qquad \text{on } \overline{D_{\text{el}}} \ , \qquad\qquad (2.1)$$

that fixes the potential on the electrode; below we are going to scale the heat source resulting from the electric field according to the actual voltage which is imposed by the generator. Furthermore, as outer boundary conditions for (1) we consider the Dirichlet boundary condition

$$\phi = 0 \qquad\qquad \text{on } B \ . \qquad\qquad (2.2)$$

Due to the electric resistance of the tissue, the potential ϕ induces a heat source Q_{rf}. However, the magnitude of this heat source depends on the power of the generator and the impedance (resistance) of the tissue, which leads to a decreased energy input if the impedance increases. To model this dependence on the characteristics of the generator we take the equivalent circuit diagram shown in Fig. 2 into account [3]. This yields a characteristic curve of the generator of the type presented in Fig. 2. The curve shows that depending on the resistance of the tissue the effective power applied to the tissue is in general smaller than the maximum power of the generator.

To provide the reader with a better perspective on how this non-linear relationship impacts the system, we provide more details on the coupling: The impedance R of the tissue is given by

$$R = \frac{U^2}{P_{\text{total}}} \quad \text{with} \quad P_{\text{total}} = \int_D \sigma|\nabla\phi|^2 \, dx \ , \qquad\qquad (3)$$
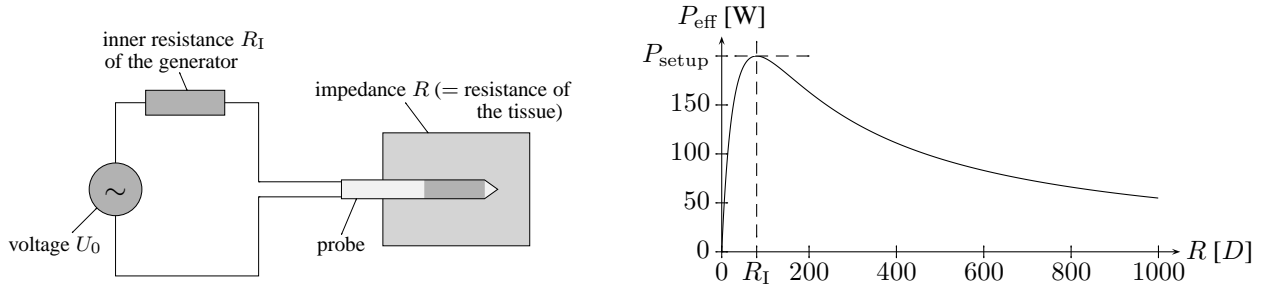
Figure 2: Left: Equivalent circuit diagram for the calculation of the scaling factor which is needed to convert the unscaled power P into the effective heat source Q_{rf}. Right: The characteristic curve of the generator shows the dependence of the effective power P_{eff} on the impedance R of the tissue, while R_I and P_{setup} are fixed (here: $R_I = 80\,\Omega$, $P_{setup} = 200\,W$).

where $U = 1\,V$ is the potential ϕ of the electrode (cf. (2.1)). According to the equivalent circuit diagram shown in Fig. 2, the effective power of the generator is now given by

$$P_{eff} = \frac{4 P_{setup} R R_I}{(R + R_I)^2} \ , \tag{4}$$

where R_I is the inner resistance of the generator and P_{setup} is the value set up at the generator's control unit. Finally, the heat source is given by

$$Q_{rf}(x) = \frac{P_{eff}}{P_{total}}\, \sigma(x)|\nabla\phi(x)|^2 \qquad \text{in } D \ , \tag{5}$$

which is proportional to the square of the magnitude of the electric field $\nabla\phi$ imposed by the electric potential ϕ.

The heat distribution $T : D \to \mathbb{R}$ is modeled by the steady state of the *Bioheat-Transfer-Equation*

$$-\mathrm{div}(\lambda(x)\nabla T(x)) = Q_{rf}(x) + Q_{perf}(x) \qquad \text{in } D \ . \tag{6}$$

Here, $\lambda : D \to \mathbb{R}$ is the thermal conductivity of the tissue. Again in our first step towards optimization, we only take spatial variation of the heat conductivity into account. More refined models also consider the dynamics of the heat distribution and the dependence of λ on other states (water content, protein state) of the system [47]. The right-hand-side of (6) consists of the source (heating) Q_{rf} due to the electric current and the sink (cooling) Q_{perf} due to the blood flow in the vascular structures D_v. We assume that there is no heating on the outer boundary of D, i.e., we choose D to be sufficiently large (cf. also Sect. 4). Thus, we consider the Dirichlet boundary condition

$$T = T_{body} \qquad \text{on } B \ . \tag{7}$$

To model the cooling effects of the blood perfusion, we use a weighted variant of the approach of Pennes [48]:

$$Q_{perf}(x) = -\nu(x)\left(T(x) - T_{body}\right) \ , \qquad\qquad \nu(x) = \begin{cases} \nu_{vessel}\, \rho_{blood}\, c_{blood} \ , & \text{if } x \in D_v \ , \\ \nu_{cap}\, \rho_{blood}\, c_{blood} \ , & \text{else} \ . \end{cases} \tag{8}$$

Thus, the coefficient $\nu : D \to \mathbb{R}$ depends on the relative blood circulation rate ν_{vessel} [s^{-1}] of vessels and ν_{cap} [s^{-1}] of capillaries respectively, as well as on the blood density ρ_{blood} [kg/m] and the heat capacity c_{blood} [$J/kg\,K$] of blood. Here, we assume that the whole tissue is pervaded by capillary vessels and thus is exposed to their cooling influence. We emphasize that for the modeling of blood flow we have again purposely chosen a very simple approach.

Remark   The modeling of perfusion has been investigated by many authors [49–53]. Sheu [54] *et al.* investigate the influence of different heat transfer coefficients between tissue and vessels. These authors conclude that with increasing ablation time the relative influence of cooling through blood advection decreases, whereas the capillary/diffusive cooling increases. Obviously, the unknown heat transfer coefficients between tissue and blood flow pose another important source of uncertainty in the simulation of RF ablation. We emphasize that, the stochastic finite element method is capable of handling these uncertain heat transfer coefficients in the bio-heat transfer equation. However, in the present work we did not investigate this uncertainty. We also note that taking into account uncertainty in flow simulations with e.g., the Navier-Stokes equations is a more involved topic which has been investigated in e.g., [32]

Remark   In the literature it is common to estimate the damage inflicted to the tissue through the temperature profile by the Arrhenius formalism [55]. This formalism considers a history integral over a certain function of the temperature, thus it takes into account that already at low temperatures (in the range of a high fever, i.e., $T \gtrsim 43\,°\mathrm{C}$) destruction of tumor cells takes place. A different approach considers a critical temperature, i.e., the temperature at which (according to the Arrhenius formalism) the tissue is destroyed after an exposure time of $1\,\mathrm{s}$. Clearly, using this approach is much simpler; however the size of lesions is underestimated.

In summary, the states $\phi : D \to \mathbb{R}$ and $T : D \to \mathbb{R}$ are defined by the boundary value problems

$$-\mathrm{div}(\sigma(x)\nabla\phi(x)) = 0 \qquad\qquad \text{in } D \setminus \overline{D_{\mathrm{el}}}, \qquad (9.1)$$
$$-\mathrm{div}(\lambda(x)\nabla T(x)) + \nu(x)T(x) = Q_{\mathrm{rf}}(x) + \nu(x)T_{\mathrm{body}} \qquad \text{in } D \qquad (9.2)$$

with boundary conditions (2) and (7). Note that the two equations are coupled through the term Q_{rf}.

2.2 Discretization

For the discretization of the elliptic boundary value problems (9.1) and (9.2) with boundary conditions (2) and (7) we use a composite FE (CFE) approach on the three dimensional uniform Cartesian grids induced by the underlying medical image data. The main advantage of CFEs over the classical FE approach is a better resolution of the RF probe's geometry. In fact, with CFEs the geometry of the RF probe is built into the shape of the basis functions, which yields high resolution of the probe even on structured grids, allowing for a combination of the adaptivity and the efficiency of structured hexahedral grids. Furthermore, in our numerical experiments we determined that good resolution of the RF probe has a significant impact on the robustness of the optimization of the RF probe placement, which will be described later. For details on the CFE method we refer the reader to [56–58].

For reasons of analogy we restrict the following description to the problem (9.2) which we assume to be adjusted to homogeneous boundary conditions in the usual way. We obtain the weak form by multiplying the corresponding PDE with a test function v. Integration by parts leads to

$$(\lambda\nabla T, \nabla v)_{2,D} + (\nu T, v)_{2,D} = (Q_{\mathrm{rf}} + \nu T_{\mathrm{body}}, v)_{2,D} \qquad (10)$$

for all test functions v, where $(\cdot, \cdot)_{2,D}$ denotes the L^2 scalar product over D.

In a second step we discretize this variational problem by restricting (10) to a finite dimensional space V^h consisting of piecewise trilinear, globally continuous shape functions of our finite element space. Note, that our CFE basis functions are adapted on the boundary of the RF probe, such that the probe's geometry is approximated sufficiently well on the grid.

Denoting the vector of nodal values t_i of the temperature with $\vec{t} = (t_1, \ldots, t_n)^T$ and the vector of nodal values r_i of the right hand side with $\vec{r} = (r_1, \ldots, r_n)^T$ we finally have to solve

$$(\mathbf{L}[\lambda] + \mathbf{M}[\nu])\,\vec{t} = \vec{r}\ ,$$

where the *stiffness matrix* $\mathbf{L}[\lambda]$ and the *mass matrix* $\mathbf{M}[\nu]$ are given by:

$$L_{ij}[\lambda] = (\lambda \nabla \psi_i, \nabla \psi_j)_{2,D} \quad \text{and} \quad M_{ij}[\nu] = (\nu \psi_i, \psi_j)_{2,D} \ .$$

Since the matrix $(\mathbf{L}[\lambda] + \mathbf{M}[\nu])$ is symmetric and positive definite, this system can be solved by e.g., a conjugate gradient (CG) method.

2.3 Optimizing the Probe Placement

The aim of the RF ablation therapy is the complete destruction of the lesion including a sufficiently large safety margin. Thus, for a given lesion it must be decided by the attending doctor how to place the RF probe such that this goal is achieved. In this section we review and extend an earlier work [9–11], which uses mathematical optimization to find the best probe placement. Our exposition in this section is the basis for an analysis of the sensitivity of the optimization with respect to the uncertainty related to the material parameters.

In the following we focus on an objective function which measures the "quality" of a given temperature distribution, i.e., which estimates the success that would be obtained with a given probe placement. For reasons of stability and robustness of the optimizer, we base our objective functional directly on the temperature profile. Thus, we relate our approach to the notion of critical temperature, having in mind that we (systematically) underestimate the size of lesions (see remark above).

For the optimization we consider an optimal ablation result to be a maximum volume of destroyed tissue, which is obtained by high temperatures inside the lesion D_{t}. Thus, to maximize the volume of ablated tissue we would therefore want to maximize the lowest temperature inside the lesion including a safety margin. Since we do not aim at an optimization of the generator power P_{setup}, it does not make sense to directly consider the deviations from a critical temperature. In fact the critical temperature would only change our chosen objective function by a constant term (see [11]).

To be more precise, let us remember that admissible probe parameters lie in the space $U := D \times S^2$. Thus, we aim at finding the optimal probe placement $(\bar{p}, \bar{a})$ such that

$$(\bar{p}, \bar{a}) = \underset{(p,a) \in U}{\operatorname{argmax}} \ \underset{x \in D_{\mathrm{t}}}{\min} \ T(x) = \underset{(p,a) \in U}{\operatorname{argmin}} \ \left(- \underset{x \in D_{\mathrm{t}}}{\min} \ T(x) \right) ,$$

where T depends on the probe placement (p, a). This objective is designed such that the smallest temperature that is attained inside the lesion is maximized. Since the $\min$-function is not differentiable it is popular to approximate it by a smooth function. In the following we use the approximation

$$\tilde{f}(T) := \frac{1}{\alpha} \log \left(\frac{1}{|D_{\mathrm{t}}|} \int_{D_{\mathrm{t}}} \exp\big(- \alpha T(x) \big) \, dx \right) \tag{11}$$

for some $\alpha > 0$. Note that for $\alpha \to \infty$, the integrand $\exp(-\alpha T(x))$ converges to zero slowest for the smallest value of $T(x)$. Thus, for large α the integrand can be approximated by the constant value $\exp(-\alpha \min_{D_{\mathrm{t}}} T)$. Consequently for large α the integral reduces to $\alpha^{-1} \log(|D_{\mathrm{t}}|^{-1} \int_{D_{\mathrm{t}}} \exp(-\alpha \min_{D_{\mathrm{t}}} T) \, dx)$, and $\tilde{f}(T)$ simplifies to $- \min_{D_{\mathrm{t}}} T$.

With our choice of approximation (11), which uses the exponential function, we seek an equal heat distribution inside the tumor, since therewith the lowest temperature inside the tumor is penalized most. The factor $\alpha > 0$ models the grade of penalization of a non-uniform temperature distribution inside the tumor.

We can write $\tilde{f}(T) = K + \alpha^{-1} f(T)$ with $K = \alpha^{-1} \log(1/|D_{\mathrm{t}}|)$ and thus arrive at

$$f(T) := \log \left(\int_{D_{\mathrm{t}}} \exp\big(- \alpha T(x) \big) \, dx \right) , \tag{12}$$

which is a simpler objective function than $\tilde{f}$. Consequently our optimization problem becomes

$$(\bar{p}, \bar{a}) = \underset{(p,a) \in U}{\operatorname{argmin}} \ f(T) = \underset{(p,a) \in U}{\operatorname{argmin}} \ \log \left(\int_{D_{\mathrm{t}}} \exp\big(- \alpha T(x) \big) \, dx \right) \ .$$

Formally, our objective function f defined above is a function of the temperature distribution T. But T depends on the heat source Q_{rf}, and Q_{rf} depends on the optimization parameter $(p, a) =: u \in U$. We can handle these dependencies by expressing our optimization problem as follows: we seek a positioning u such that the cost function given in terms of the positioning $F(u) = f \circ \mathcal{T} \circ \mathcal{Q}(u)$ is minimized where

$$\mathcal{Q}(u) = Q_{\mathrm{rf}} \ , \quad T = \mathcal{T}(Q_{\mathrm{rf}}) \ .$$

Obviously, in certain situations the uniqueness of a minimizing configuration is not guaranteed, e.g., for spherical tumors. This situation may also occur in practice for hepatic tumors which in general have a spherical-like shape. However, such a symmetry is broken by the consideration of surrounding blood vessels and their cooling effects. Moreover, for practical reasons the uniqueness of a solution is not needed and even local minima give important information about good probe and generator configurations. In a future model we will incorporate constraints for the optimization parameters which break any existing symmetry even further. Such constraints are given by anatomical structures (bones, colon, diaphragm) that must not be punctured during the ablation.

2.4 Multiscale Gradient Descent

For the minimization of the objective functional F, we use a gradient descent method. Since the orientation a lies on the two-dimensional sphere S^2 and the computation of a gradient on the sphere would involve some difficulties (in particular because there is no basis of the tangent space of S^2 at a that depends continuously on a), we replace U by the open set

$$\tilde{U} = D \times (\mathbb{R}^3 \setminus \{0\}) \supset U \ ,$$

and use in each step of the gradient descent method the projection

$$P_{D \times S^2} : \tilde{U} \to U \ , \qquad\qquad (p, a) \mapsto (p, a/|a|) \ .$$

We also define a continuation of or solution operator $\mathcal{Q}$ onto $\tilde{U}$ that does not depend on the length of a via

$$\mathcal{Q}(p, a) = (\mathcal{Q} \circ P_{D \times S^2})(p, a) = \mathcal{Q}(p, a/|a|) \ .$$

Letting the superscript $n \in \mathbb{N}$ denote the iteration count, we can describe the particular ingredients of our gradient descent method as follows:

- **Initial value.** Set $n = 0$, and choose an arbitrary probe positioning $u^0 \in U$ as an initial guess.

- **Descent direction.** Then, in each iteration step $n \geq 1$, calculate the descent direction $w^n \in \tilde{U}$ from the current iterate u^n as an approximation of $-D_u F(u^n)$, i.e., $-D_u(f \circ T \circ Q_{\mathrm{rf}}(u^n))$.

- **Step size.** Determine the step size $s^n > 0$, such that the resulting new iterate $u^{n+1} = P_{D \times S^2}(u^n + s^n w^n)$ is admissible, i.e., fulfills $u^{n+1} \in U$ and reduces the value of the objective function $F(u^{n+1}) < F(u^n)$. Using the projection $P_{D \times S^2}$, we assert that the new orientation lies on the sphere.

- **Stopping criterion.** The iteration continues until the difference $|u^{n+1} - u^n|$ falls below a given threshold θ.

To accelerate the gradient descent algorithm, we use a multi-scale approach, i.e., we start with the optimization on a coarse grid and use the solution as the initial guess on a finer grid. In Alg. 1 we show the complete multi-scale optimization algorithm in pseudo-code. For each level l (see lines 3–25 of Alg. 1) of the computational grid the optimization is performed as described above. The descent direction w^n in line 7 of Alg. 1 is computed with help of a conjugate gradient calculation of the corresponding adjoint equation (see [9–11]) and a determination of the derivative of the heat source Q_{rf} with respect to the probe positioning u via shape derivatives (see [11]). Specifically,

---

Algorithm 1 Multi-scale gradient descent for the optimization of the probe placement

---

1: $l \leftarrow l_0$ ▷ Start with level l_0

2: Initialize $\bar{u}$.

3: **while** $l \leq L$ **do**

4:      $u^0 \leftarrow \bar{u}$ ▷ Initialization

5:      $n \leftarrow 0$

6:      **repeat**

7:          $w^n \leftarrow -\nabla_u F(u^n) = -D_u f(T(Q_{\mathrm{rf}}(u^n)))$ ▷ Compute descent direction

8:          **if** $n = 0$ **then**   ▷ Initialize step size

9:              $s^0 \leftarrow (2|w^0|)^{-1}\mathrm{diam}(D)$

10:         **else**

11:             $s^n \leftarrow 2|w^{n-1}|(|w^n|)^{-1}s^{n-1}$

12:         **end if**

13:         $m \leftarrow 0$ ▷ Reset counter

14:         $u^{n+1} \leftarrow P(u^n + s^n w^n)$ ▷ Determine step size

15:         **while** $F(u^{n+1}) > F(u^n)$ or $u^{n+1} \notin U$ **do**

16:             $m \leftarrow m + 1$ ▷ Increase counter

17:             **if** $m = m_{\max}$ **then**

18:                STOP

19:             **end if**

20:             $s^n \leftarrow s^n / 2$ ▷ Bisect step size

21:             $u^{n+1} \leftarrow P(u^n + s^n w^n)$

22:         **end while**

23:      **until** $|u^{n+1} - u^n| \leq \theta$

24:      $\bar{u} \leftarrow u^{n+1}$

25:      $l \leftarrow l + 1$ ▷ Proceed to next level

26: **end while**

---

we interpret the probe placement $u \in \tilde{U}$ as a vector of shape parameters $p \in \mathbb{R}^6$ such that the computational domain D depends on p, i.e., $D = D(p)$ and in particular $D_{\mathrm{el}} = D_{\mathrm{el}}(p)$. Then we can calculate $\partial_{p_i} Q_{\mathrm{rf}}$ as

$$
\partial_{p_i} Q_{\mathrm{rf}} = \partial_{p_i} \left(\frac{P_{\mathrm{eff}}}{P_{\mathrm{total}}} \, \sigma |\nabla \phi|^2 \right)
$$

$$
= \sigma \left(-2 \int_D \sigma \nabla \phi \nabla(\partial_{p_i} \phi) dx \left(P_{\mathrm{eff}} + P_{\mathrm{eff}} \frac{R_I - R}{R(R + R_I)} \frac{U^2}{P_{\mathrm{total}}} \right) \frac{|\nabla \phi|^2}{P_{\mathrm{total}}^2} + 2 \frac{P_{\mathrm{eff}}}{P_{\mathrm{total}}} \nabla \phi \nabla(\partial_{p_i} \phi) \right) \quad .
$$

Here, the derivative $\partial_{p_i} \phi$ of the potential ϕ with respect to the shape parameter p_i is calculated by the following PDE system obtained by a transformation of the potential equation (1) with boundary conditions (2)

$$
\int_{D \setminus D_{\mathrm{el}}} \sigma \langle \nabla \partial_{p_i} \phi, \nabla v \rangle dx = 0
$$

$$
\partial_{p_i} \phi = -\langle \nabla \phi, x_{p_i} \rangle \quad \forall \, x \in \partial D_{\mathrm{el}} \quad .
$$

For the integration in the objective function we use a tensor-product trapezoidal rule. The search for the optimal step size is performed with a variant of Armijo's rule (cf. e.g., [39]) (lines 8–22 of Alg. 1). Note that for each test

in the while-condition (see Alg. 1, line 15), an evaluation of the complete system of PDEs (9), and the objective function are needed. To obtain representations of the vascular structure D_v and of the lesion D_t on coarse grids we use a bilinear restriction frequently used in multi-grid methods [59] with an additional threshold for the tumor and the vessels to obtain sharp boundaries.

For more details of the multi-scale gradient descent approach we refer the reader to [10]. There, we have also verified the multi-scale optimization process on the basis of an artificial example where the optimal probe placement is qualitatively known.

3. MATERIAL PARAMETER UNCERTAINTY

The PDE model for the simulation of the heat distribution described in the last section involves the electric and thermal conductivity of the corresponding tissue. As we have discussed in the introduction, we must note that these quantities cannot be determined exactly. The material properties depend on the physical state of the tissue, and moreover they vary inter-individually (i.e., from patient to patient) and in fact they also vary from day to day depending on the patients physical constitution. The range of values, which are given in the literature, underline this uncertainty, e.g., from [3, 4, 6, 8] we learn that even in native liver tissue we have

$$\sigma = 0.17\,\mathrm{S/m}\text{---}0.60\,\mathrm{S/m}\ ,\qquad \lambda = 0.47\,\mathrm{W/Km}\text{---}0.64\,\mathrm{W/Km}\ . \tag{13}$$

These values have mostly been obtained from *in vitro* experiments on cadaveric human tissue or animals, and they are certainly furthermore associated with realistic measurement errors of 10% or more.

Taking the uncertainty of the values of material parameters into account leads to the question about the dependence of the forward simulation of RF ablation and also about the sensitivity of the optimal probe placement found in Sect. 2 with respect to variations (either due to uncertainty or errors) in the material parameters. Discussing this question does not improve the accuracy of the simulation or the optimization (as numerical verification is a matter divorced from the answer to this question); rather, it enables us to quantify how the uncertainty of the electric and thermal conductivities affects (or propagates through) the numerical results. Based on the results obtained by our sensitivity analysis, a future goal in direction of a patient-specific modeling and simulation will be the optimization of the confidence of the success of the therapy.

In the following, we extend the model for the simulation and optimization of RF ablation presented in Sect. 2 such that it incorporates the uncertainty in the material properties. In Sect. 3.2 we give a brief overview of some common methods for the stochastic discretization and in particular describe the stochastic finite element method with piecewise multilinear ansatz functions, which we use in this work. Further we discuss three different variants to analyze the sensitivity of the optimal probe placement in Sect. 3.3.

3.1 A Stochastic Model for RF Ablation

Let $(\Omega, \mathcal{A}, \mu)$ be a probability space expressing the behavior of the thermal conductivity and electric conductivity where Ω is the event space, $\mathcal{A} \subset 2^{\Omega}$ the σ-algebra, and μ the probability measure. In the following we consider the case that the tissue parameters σ and λ are not fixed to particular (deterministic) values, but rather lie within a range of possible values. Thus, an event ω in our probability space consists of a particular choice of the material properties (σ, λ). The physical parameters can be considered as random fields expressible in terms of random variables and characterizable by their probability density functions (PDFs).

For the medical problem of interest, let us assume that we have three main types of tissue present in our computational domain: native liver tissue (n), tumor tissue (t), and blood vessels (v). For each of these tissue types we assume that the distribution of σ and λ are controlled by uniformly distributed independent random variables, each of which is defined over the interval $[-1, 1]$.

Following [60], we know that we can represent any general second-order *random process* $g(\omega)$, $\omega \in \Omega$ in terms of a collection of random variables $\boldsymbol{\xi} = (\xi_1, \dots \xi_N)$ with independent components. Here, the stochastic process under investigation is the optimal probe placement $\bar{u}$ as it is obtained by the algorithm described in the previous section. Since the optimal probe placement depends on the material parameters σ and λ any uncertainty associated with those

parameters will induce uncertainty in the optimal probe placement. Note that in the following we will also refer to *random fields* as stochastic processes.

Remark   Here and in the following we assume that the distributions for the three-different components of the material parameters are independent. Note that from the mathematical viewpoint it is very convenient to assume independence since it allows to construct tensor-product Hilbert spaces on the stochastic domain. Note independence may not be justified from the anatomical perspective, since e.g., the different conductivities are correlated through the water content of the tissue. However, there exists a mathematically rigorous (nonlinear) mapping which transforms a set of random variables into a set of independent random variables. This research falls into the area of numerical representation of non-Gaussian processes, which remains an active research field [34].

To describe the electric field emerging from the RF probe regarded as a random field, let us consider the vector of random variables $\boldsymbol{\xi}^\sigma = (\xi_n^\sigma, \xi_t^\sigma, \xi_v^\sigma) \in \Gamma_\sigma := [-1, 1]^3$ (i.e., $N = 3$) which describes the uncertainty in the electric conductivity of the native tissue, the tumor, and the vessels. We model the stochastic field $\sigma(x, \boldsymbol{\xi}^\sigma)$ for the uncertain electric conductivity by

$$\sigma(x, \boldsymbol{\xi}^\sigma) = \begin{cases} \sigma_n(\xi_n^\sigma) & \text{if } x \in D_n \ , \\ \sigma_t(\xi_t^\sigma) & \text{if } x \in D_t \ , \\ \sigma_v(\xi_v^\sigma) & \text{if } x \in D_v \ . \end{cases} \tag{14}$$

To model the uncertain distribution of heat we proceed similarly by considering $\boldsymbol{\xi}^\lambda = (\xi_n^\lambda, \xi_t^\lambda, \xi_v^\lambda) \in \Gamma_\lambda := [-1, 1]^3$. The three components of $\boldsymbol{\xi}^\lambda$ represent the heat conductivity in the native and malignant tissue as well as in the vascular structures. Like in (14) we define the overall heat conductivity $\lambda(x, \boldsymbol{\xi}^\lambda)$. We will henceforth consider our input parameters to be of the form $\sigma(x, \boldsymbol{\xi}^\sigma)$ and $\lambda(x, \boldsymbol{\xi}^\lambda)$ given by $\boldsymbol{\xi} = (\boldsymbol{\xi}^\sigma, \boldsymbol{\xi}^\lambda) \in \Gamma$ distributed over the ranges as e.g., given in (13), where $\Gamma := \Gamma_\sigma \times \Gamma_\lambda = [-1, 1]^3 \times [-1, 1]^3$.

Having introduced the uncertain electric conductivity, we can formulate a *stochastic electrostatic equation* similar to (1) and (2) by: Find a stochastic field $\phi(x, \boldsymbol{\xi}^\sigma)$ such that

$$\begin{aligned} -\text{div}(\sigma(x, \boldsymbol{\xi}^\sigma)\, \nabla\phi(x, \boldsymbol{\xi}^\sigma)) &= 0 & \text{a.e. in } D \setminus \overline{D_{\text{el}}} \times \Gamma_\sigma \ , \\ \phi(x, \boldsymbol{\xi}^\sigma) &= 1 & \text{a.e. on } \overline{D_{\text{el}}} \times \Gamma_\sigma \ , \\ \phi(x, \boldsymbol{\xi}^\sigma) &= 0 & \text{a.e. on } \partial D \times \Gamma_\sigma \ . \end{aligned} \tag{15}$$

Straightforwardly, we can proceed to incorporate the uncertainty into the remaining components of the model that has been presented in Section 2.1. This yields a stochastic field for the heat source and stochastic processes for the total and the effective power, i.e.,

$$Q_{\text{rf}}(x, \boldsymbol{\xi}^\sigma) = \frac{P_{\text{eff}}(\boldsymbol{\xi}^\sigma)}{P_{\text{total}}(\boldsymbol{\xi}^\sigma)} \ \sigma(x, \boldsymbol{\xi}^\sigma)|\nabla\phi(x, \boldsymbol{\xi}^\sigma)|^2 \ , \tag{16}$$

$$P_{\text{eff}}(\boldsymbol{\xi}^\sigma) = \frac{4P_{\text{setup}}R(\boldsymbol{\xi}^\sigma)R_{\text{I}}}{(R(\boldsymbol{\xi}^\sigma) + R_{\text{I}})^2} \ , \quad R(\boldsymbol{\xi}^\sigma) = \frac{U^2}{P_{\text{total}}(\boldsymbol{\xi}^\sigma)} \ , \quad P_{\text{total}}(\boldsymbol{\xi}^\sigma) = \int_D \sigma(x, \boldsymbol{\xi}^\sigma)|\nabla\phi(x, \boldsymbol{\xi}^\sigma)|^2 \, dx \ . \tag{17}$$

We may also define the *stochastic heat equation* in analogy to (6) and (7). Since the source term on the right hand side depends on the solution of the stochastic electrostatic equation, the temperature distribution is going to be a random field that depends on both $\boldsymbol{\xi}^\sigma$ and $\boldsymbol{\xi}^\lambda$, i.e.,

$$\begin{aligned} -\text{div}(\lambda(x, \boldsymbol{\xi}^\lambda)\nabla T(x, \boldsymbol{\xi})) &= Q_{\text{rf}}(x, \boldsymbol{\xi}^\sigma) + Q_{\text{perf}}(x, \boldsymbol{\xi}) & \text{a.e. in } D \times \Gamma \ , \\ T(x, \boldsymbol{\xi}) &= T_{\text{body}} & \text{a.e. on } \partial D \times \Gamma \ , \end{aligned} \tag{18}$$

where $\boldsymbol{\xi} = (\boldsymbol{\xi}^{\sigma}, \boldsymbol{\xi}^{\lambda})$. The sink term Q_{perf} in (18) is modeled like in Section 2.1

$$Q_{\mathrm{perf}}(x, \boldsymbol{\xi}) = -\nu(x)\,(T(x, \boldsymbol{\xi}) - T_{\mathrm{body}})\ ,\qquad \nu(x) = \begin{cases} \nu_{\mathrm{vessel}}\,\rho_{\mathrm{blood}}\,c_{\mathrm{blood}} & \text{for } x \in D_{\mathrm{v}}\ , \\ \nu_{\mathrm{cap}}\,\rho_{\mathrm{blood}}\,c_{\mathrm{blood}} & \text{else}\ . \end{cases} \qquad (19)$$

3.2 Stochastic Discretization

In the following we give a short overview of some common methods for the stochastic discretization (see also [44]). We start with the Monte Carlo (MC) method, then proceed to a description of the stochastic Galerkin (SG) method and finally mention the stochastic collocation method and the stochastic finite element method (SFEM) with piecewise multilinear ansatz functions, as used in our sensitivity analysis.

3.2.1 Monte Carlo Simulation

A classical and very popular approach for the stochastic discretization is the Monte Carlo (MC) method. Thereby P realizations $\boldsymbol{\xi}_j,\ j = 1,\ldots,P$ of the vector of random variables $\boldsymbol{\xi}$ are generated. Consequently, P deterministic problems are solved, which are obtained from (15) and (18) by considering the realizations of the electric and thermal conductivity σ and λ corresponding to $\boldsymbol{\xi}_j$. Finally, the statistics of the solution samples $T_j = T(x, \boldsymbol{\xi}_j)$, or of the corresponding samples of the optimal probe placement $\bar{u}(\boldsymbol{\xi}_j) = (\bar{p}(\boldsymbol{\xi}_j), \bar{a}(\boldsymbol{\xi}_j))$ obtained by the optimization presented in Sect. 2, lead to the desired result. The MC approach is known to be extremely robust and requires no assumptions on the smoothness of the underlying stochastic processes. However, the convergence is very slow and goes asymptotically with $1/\sqrt{P}$.

3.2.2 Stochastic Galerkin Method

The stochastic Galerkin method utilizes the weak formulation of (15) and (18) on finite dimensional stochastic subspaces of the probabilistic Hilbert space, in which the random processes lie. The approximating subspaces can be constructed by e.g., the generalized Polynomial Chaos (gPC) approach. Thereby any second-order stochastic process $g(\boldsymbol{\xi})$ written in terms of random variables, is represented by a weighted (infinite) sum of orthogonal polynomials [31, 32, 61, 62] which are functions of the vector of random variables $\boldsymbol{\xi}$ of known probability density function (PDF). Here, in the case of this study, the random input fields of interest are the (stochastic) input parameters σ and λ. The random process of interest is the optimal probe placement $\bar{u}$ for which we solve in Section 2.

An approximation of a stochastic process can be expressed by truncating the infinite summation to $P + 1$ terms for some $P \in \mathbb{N}$. Denoting the stochastic orthogonal polynomial set as $L_i(\boldsymbol{\xi})$ and the polynomial weights as $\hat{g}_i$, we can write our approximation of the process as

$$\tilde{g}(\boldsymbol{\xi}) = \sum_{i=0}^{P} \hat{g}_i L_i(\boldsymbol{\xi})\ ,\quad \text{with}\quad \hat{g}_i = \left(\int_{\Gamma} L_i^2\,d\mu(\boldsymbol{\xi})\right)^{-1} \int_{\Gamma} g(\boldsymbol{\xi}) L_i(\boldsymbol{\xi})\,d\mu(\boldsymbol{\xi})\ . \qquad (20)$$

In the case of random processes g that depend on a scalar random variable ξ (e.g., $\sigma_{\mathrm{m}}(\xi_{\mathrm{m}}^{\sigma})$, $\mathrm{m} \in \{\mathrm{n, t, v}\}$, cf. (14)) and which have uniform distribution, the Legendre polynomials are the optimal orthogonal polynomials to employ [62]; this allows us to express $g(\xi)$ exactly in terms of two coefficients such that $g(\xi) = \hat{g}_0 L_0(\xi) + \hat{g}_1 L_1(\xi) = \hat{g}_0 + \hat{g}_1 \xi$, where the first coefficient is the midpoint of the uniform interval and the second coefficient is the half-length of the uniform interval.

3.2.3 Stochastic Collocation Method

In the generalized polynomial chaos - stochastic collocation (gPC-SC) approach [63] quadrature rules are employed which collocate the stochastic process of interest for accomplishing the integration over the stochastic domain in order to compute the coefficients $\hat{g}_i$ of the expansion (20). It is popular to use a set of quadrature points $\{\boldsymbol{\xi}_j\}_{j=1}^{Q}$ which lie on a sparse grid in the stochastic space (see Fig. 3, left) generated by Smolyak's algorithm [63].

Analogous to a classical polynomial interpolation, the use of Lagrange interpolation is particularly convenient: Instead of using the collocation points $\boldsymbol{\xi}_j$ for an integration of the coefficients in the expansion (20), an approximation of the stochastic process on the incomplete polynomial space resulting from Smolyak's algorithm is considered. Thus, the interpolation approximation of $f(\boldsymbol{\xi})$ can be defined by

$$\tilde{f}(\boldsymbol{\xi}) = \sum_{j=1}^{Q} f(\boldsymbol{\xi}_j) h_j(\boldsymbol{\xi}) = \sum_{j=1}^{Q} \mathcal{F}(g(\boldsymbol{\xi}_j)) h_j(\boldsymbol{\xi}) \tag{21}$$

with a set of Lagrange interpolating basis functions $h_i(\boldsymbol{\xi}_j) = \delta_{ij}$. Here $\mathcal{F}$ denotes the solution operator for the deterministic model from the previous sections, i.e., $f(\boldsymbol{\xi}) = \mathcal{F}(g(\boldsymbol{\xi}))$. Solving the deterministic system at the collection of samples $\{\boldsymbol{\xi}_j\}_{j=1}^{Q}$ allows one to construct an approximation such that the residual $R(f(\boldsymbol{\xi}) - \tilde{f}(\boldsymbol{\xi}))$ between the interpolated system $\tilde{f}(\boldsymbol{\xi})$ and the true process $f(\boldsymbol{\xi})$ is zero at these points.

With the interpolation (21) an approximation of the mean of the process $f(\boldsymbol{\xi})$ is given by

$$\bar{f} = \mathbb{E}[(f)(\boldsymbol{\xi})] = \int_{\Gamma} f(\boldsymbol{\xi}) d\mu(\boldsymbol{\xi}) \approx \sum_{j=1}^{Q} w_j f(\boldsymbol{\xi}_j) = \sum_{j=1}^{Q} w_j \mathcal{F}(g(\boldsymbol{\xi}_j)) \ , \tag{22}$$

where w_j are the collocation weights derived by integration of the interpolation functions $w_j = \int_{\Gamma} h_j(\boldsymbol{\xi}) d\mu(\boldsymbol{\xi})$. Similarly, an approximation of the variance can be calculated as follows:

$$\mathrm{Var}[f(\boldsymbol{\xi})] \quad = \quad \mathbb{E}[(f(\boldsymbol{\xi}) - \bar{f})^2] \approx \sum_{j=1}^{Q} w_j (f(\boldsymbol{\xi}_j) - \bar{f})^2 \ . \tag{23}$$

Let us finally note that the collocation approach discussed above is one of multiple possible collocation methods used in the solution of stochastic PDEs [64]. With increasing rate of convergence (and increasing assumptions on smoothness) one can use approaches based e.g., on the classical Monte-Carlo method, the Newton-Cotes formulas, Gaussian or Clenshaw-Curtis quadrature, or the sparse-grid spectral collocation method discussed here.

3.2.4 Stochastic Finite Element Method

For the sensitivity analysis of the optimal probe placement with respect to variations in the tissue properties, here we use a slightly modified method of discretizing and numerically solving the involved SPDEs, which requires weaker smoothness assumptions on the stochastic process than the previously presented global collocation approach. More precisely, here we use a stochastic finite element method with piecewise multilinear ansatz functions on uniform hierarchical grids, which are adaptively refined in critical stochastic regions (see Fig. 3, middle). Thus, the interpolating basis functions h_j in (21) are changed to piecewise multilinear ansatz functions like the ones depicted on the right of Fig. 3, i.e., instead of orthogonal polynomials, here we take these piecewise multilinear ansatz functions for the interpolation between the adaptively refined sampling points in the stochastic space. This methodology, sometimes referred to as the collocating multi-element polynomial chaos method [37, 38] combines the advantages of the stochaatic collocation method with flexibility of a multi-element (hierarchical) approach.

3.3 Sensitivity Analysis

From the approximation of the stochastic process describing the optimal probe placement we now can analyze the sensitivity of the system to perturbations in the parameters. In the following, we discuss two different variants for the parametric sensitivity analysis through the stochastic finite element approach described above. In Section 4 we will present examples for the second of the variants discussed in the following.
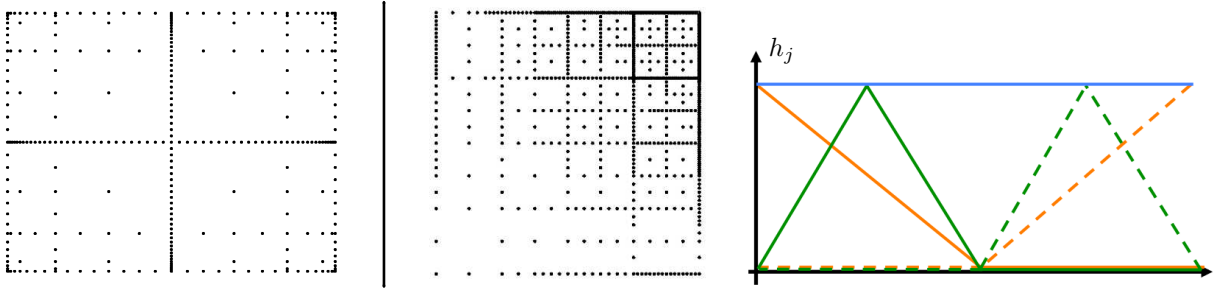
Figure 3: Left: Distribution of grid nodes obtained with Smolyak's algorithm. Middle: Uniform, adaptive distribution of nodes for the stochastic interpolation with piecewise multilinear, hierarchical ansatz functions. Right: First five piecewise linear ansatz functions h_j for the interpolation approximation of the random field $f(\xi) \approx \sum_{j=1}^{Q} f(\xi_j) h_j(\xi)$ (see (21)).

3.3.1 Probability Density of Joint Distribution

A first approach that reveals the robustness (or more precisely the global behavior) of the optimal probe placement with respect to variations in the material parameters is given by a direct analysis of the probability density function (PDF) of the probe placement.

In general, the PDF is not calculable analytically; one has to evaluate the stochastic process, i.e., the representation (21) of the random field f with piecewise multilinear ansatz functions h_j, at a large number of sampling points to get an appropriate approximation of the PDF. For more details we refer the reader to [64] and in particular to [65].

3.3.2 Covariance of Joint Distribution

Instead of the calculation of the PDF, one can investigate the covariance matrix of the joint distribution of the components of the optimal probe placement. The covariance matrix of the approximation $\tilde{f}$ of the random field f (cf. (21) with piecewise multilinear ansatz functions h_j) can be computed much faster than the PDF, and its results are easier to interpret. Formally, the covariance matrix of the joint distribution of the coordinates of e.g., the optimal probe position $\bar{p}(\xi) = (\bar{p}_x(\xi), \bar{p}_y(\xi), \bar{p}_z(\xi))$ can be written as

$$\text{Cov}[\bar{p}] = \big(\text{Cov}[\bar{p}_c, \bar{p}_d]\big)_{c,d \in \{x,y,z\}} \quad , \quad \text{where} \quad \text{Cov}[\bar{p}_c, \bar{p}_d] = \mathbb{E}\big[(\bar{p}_c - \mathbb{E}[\bar{p}_c])(\bar{p}_d - \mathbb{E}[\bar{p}_d])\big]$$

for all pairs of coordinates $c, d \in \{x, y, z\}$. The covariance matrix is a symmetric (in this case 3×3) matrix that quantifies how the coordinates of e.g., the optimal probe position are coupled through the random variable ξ. If this matrix were diagonal, the coordinates would be independent.

Remark   We emphasize that special care must be taken concerning the accuracy of the numerical solvers involved. In [66] Kaipio and Somersalo discuss that limited numerical accuracies (i.e., discretization errors) can sometimes (effectively or ineffectively) be interpreted as the behavior of a random process and thus as sensitivity of our problem. Consequently, in our numerical experiments shown in Sect. 4 we have set the stopping criteria of the iterative solvers as well as for the optimization loops appropriately.

4. RESULTS

In the following we will evaluate the concepts presented in the preceding sections on the basis of a real RF ablation case. Here, we consider the material parameters to be uniformly distributed. The thermal conductivity $\lambda = (\lambda_n, \lambda_t, \lambda_v)$

ranges in $[0.47, 0.64] \times [0.51, 0.77] \times [0.51, 0.54]$ [W/Km]. Moreover, the electric conductivity $\sigma = (\sigma_n, \sigma_t, \sigma_v)$ ranges in $[0.17, 0.60] \times [0.64, 0.96] \times [0.67, 0.86]$ [S/m]. The respective intervals have been chosen based upon values found in the literature [3, 4, 6].

In general, to find an appropriate refinement level one can use the same procedure as for the determination of an appropriate spatial grid resolution: The respective computation is performed for a hierarchy of increasing level values and the results are tested for Cauchy convergence. For this purpose we compare the optimizer $(\bar{p}, \bar{a})$ at each node with the corresponding interpolate from the previous refinement level. We need an additional level of refinement at one node as long as the positions differ by more than $1\,\mathrm{mm}$ or the angles differ by more than $5\,°$. Below we show the results of such a hierarchy of computations for the sensitivity of the probe position w.r.t. variations in the electric conductivity.

As settings for one deterministic optimization, here we use $\alpha = 0.5$ within the objective function f in (12) and $\theta = 10^{-6}$ within the stopping criterion related to the probe position, as well as $\theta = 10^{-3}$ within the stopping criterion related to the probe orientation. For the iterative solvers used in the computation of the forward problem we use an accuracy of at least 10^{-15} for the decrease of the residual. The computational domain D is of extent $60 \times 60 \times 60\,\mathrm{mm}^3$, and it is discretized with a fine grid of 64^3 cells. For the multi-scale optimization we consider one coarser grid having 32^3 cells. With these settings the optimization of the probe location for one sampling point in the stochastic space typically takes about $2\,\mathrm{h}$ on a standard desktop PC with an Intel® Core 2 Duo™ $2.93\,\mathrm{GHz}$ processor and $4\,\mathrm{GB}$ RAM.

Here, we work with CT data which has been segmented to obtain the vascular system with a tumor of interest. The segmentation has been performed by the methods presented in [45]. The tumor located in this domain has main axes of approximate length $45.9\,\mathrm{mm}$, $41.9\,\mathrm{mm}$, and $36.2\,\mathrm{mm}$.

For the perfusion term (8) we take $\nu_{\mathrm{cap}} = 0.006067\,\mathrm{s}^{-1}$ and $\nu_{\mathrm{vessel}} = 0.05\,\mathrm{s}^{-1}$. The value for the blood density is $\rho_{\mathrm{blood}} = 1059.0\,\mathrm{kg/m^3}$, and the heat capacity of blood is set to $c_{\mathrm{blood}} = 3850.0\,\mathrm{J/kgK}$ (cf. Sect. 2 and [3, 6]).

A monopolar probe with radius $1.2\,\mathrm{mm}$ and with an electrode length of $20\,\mathrm{mm}$ is applied. The electric generator has an inner resistance of $80\,\Omega$, and it is set up to a power of $30\,\mathrm{W}$. For the optimization, the initial probe position is always located at a distance of $11.25\,\mathrm{mm}$ in each coordinate direction from the center of D. The initial orientation is $a = (5, 2, 3)$, projected on the sphere (i.e., normalized to length 1).

Remark To guarantee that the size of our computational domain does not influence the result of the optimizer, we have performed a comparison between forward simulations using Dirichlet or Neumann boundary conditions at ∂D, respectively. Both temperature profiles differ at most by $0.45\,\mathrm{K}$ in the interior of D, i.e., at locations which are more than $10\,\mathrm{mm}$ apart from ∂D. Closer to the boundary, i.e., for locations which lie in a ring with radius $10\,\mathrm{mm}$ around ∂D, the temperatures differ more. In particular, the largest deviation of $4.93\,\mathrm{K}$ appears at the outer boundary ∂D. We conclude that in the vicinity of the lesion the particular choice of boundary condition does not influence the result significantly.

4.1 Sensitivity of the Temperature

Before we analyze the sensitivity of the optimal probe position and orientation, we first investigate the sensitivity of the temperature, calculated by our forward simulation (see Sect. 2.1). More precisely, we perform a simple sampling of the six-dimensional stochastic space for stochastic σ and λ by $3^6 = 729$ grid points, such that all 3^6 combinations of σ and λ at the interval boundaries and at the middle of the intervals are considered. We then determine the values of σ and λ, for which the L^∞-norm of the temperatures differs most. In Fig. 4 we see the result of this investigation. In more detail, we see the $50\,°\mathrm{C}$ isosurface of the temperatures, whose maximal values differ most (left and middle) together with the $30\,\mathrm{K}$ isosurface of the difference of the temperatures obtained by a simple subtraction of the two temperatures from each other (right). The corresponding values for the electric and thermal conductivity are $(\sigma_n, \sigma_t, \sigma_v, \lambda_n, \lambda_t, \lambda_v) = (0.17, 0.64, 0.67, 0.64, 0.51, 0.54)$ (Fig. 4, left) and $(\sigma_n, \sigma_t, \sigma_v, \lambda_n, \lambda_t, \lambda_v) = (0.60, 0.64, 0.86, 0.47, 0.77, 0.51)$ (Fig. 4, middle). This corresponds to our expectation, since for a large value of the thermal conductivity λ_t within the tumor region (Fig. 4, middle) the high temperature
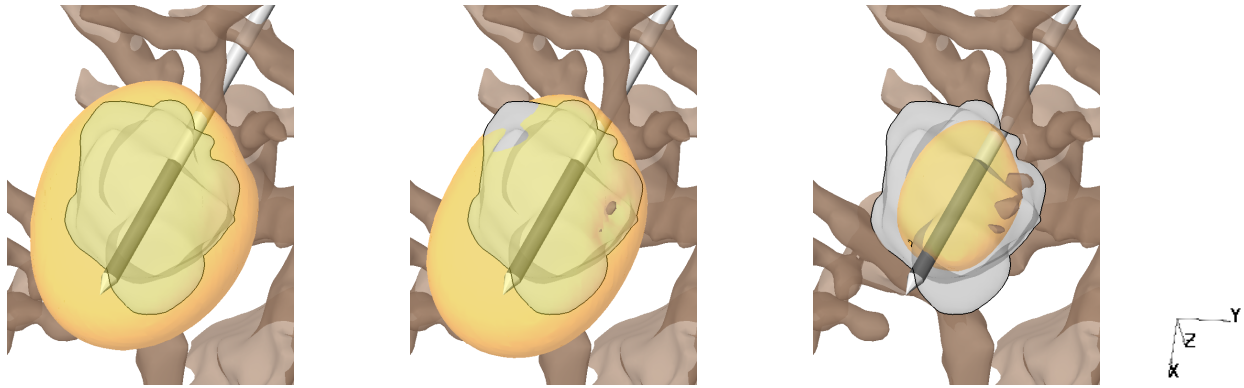
Figure 4: Left and Middle: We show the $50\,°\mathrm{C}$ isosurface of two different temperatures obtained for different realizations of σ and λ. Right: Visualization of the $30\,\mathrm{K}$ isosurface of the difference of the two temperatures, whose $50\,°\mathrm{C}$ isosurfaces are presented on the left. In all images the vascular system D_v is displayed in beige-brown and the tumor lesion D_t is displayed in a transparent gray color.

around the probe diffuses faster away than for a small value of λ_t. From the results we see a significant difference in the shape of the $50\,°\mathrm{C}$ temperature profiles, especially close by the vessels (see left and middle image of Fig. 4). Moreover, we see that the largest temperature difference appears around the end of the probe's electrode which lies close by the vascular system (see right image of Fig. 4). Further, we notice that obviously there exist material parameter settings for which a complete ablation of the tumor is not achieved (Fig. 4, middle). This further motivates the consideration of the material parameter uncertainty for the planning of RF ablation.

4.2 Sensitivity of the Optimal Probe Location

In Sect. 3.3 we have described different variants for a sensitivity analysis of the optimal probe placement with respect to variations in the material parameters. Let us first note that since the space of admissible probe placements U is a five-dimensional space, a visualization and an analysis of the PDFs of the corresponding distributions is not straightforward (cf. also [65]), because the PDFs are functions $U \to \mathbb{R}$.

When we take uncertainty in the values of σ or λ in all three tissue types (native liver tissue, tumor and vessels) into account, we have a three-dimensional stochastic space Γ. On this space we can approximate a stochastic process through stochastic finite elements that reveal the dependence of the optimal probe placement $\bar{u}$ (which lies in a five-dimensional space U; three dimensional probe location $p \in \mathbb{R}^3$ and an orientation vector $a \in S^2$ on the two-dimensional sphere) w.r.t. variations in the parameters σ or λ.

In our investigations we found that the optimization of only the probe's position with fixed orientation and the optimization of only the probe's orientation with fixed position have less local optima than the optimization of both quantities at the same time. Thus, we first analyze the sensitivity of the optimal probe position and orientation separately (i.e., independent of each other) (see Figs. 5 and 6) and as a further step then also consider the sensitivity of the simultaneous optimization of both quantities (see Fig. 7).

Let us first discuss a visualization that reduces the complexity of the data and allows for an easy perception of the distribution of the optimal probe location $\bar{p}$. The PDF of the optimal probe location is a mapping $\mathbb{R}^3 \to \mathbb{R}$ which could be visualized through a volume rendering. However, a deep understanding and analysis of the three-dimensional PDF can be obtained only by an interactive three-dimensional display of the data. Therefore we use the second approach described in Sect. 3.3 to provide a simpler and better perceptible visualization. From the probability distribution of the optimal probe location we compute the first and the second moment, corresponding to the mean and the covariance. An eigenanalysis allows us to draw an ellipsoid centered at the mean, oriented with the eigenvectors, and scaled with the square root of the eigenvalues of the covariance matrix. It can be interpreted as a principal component analysis of
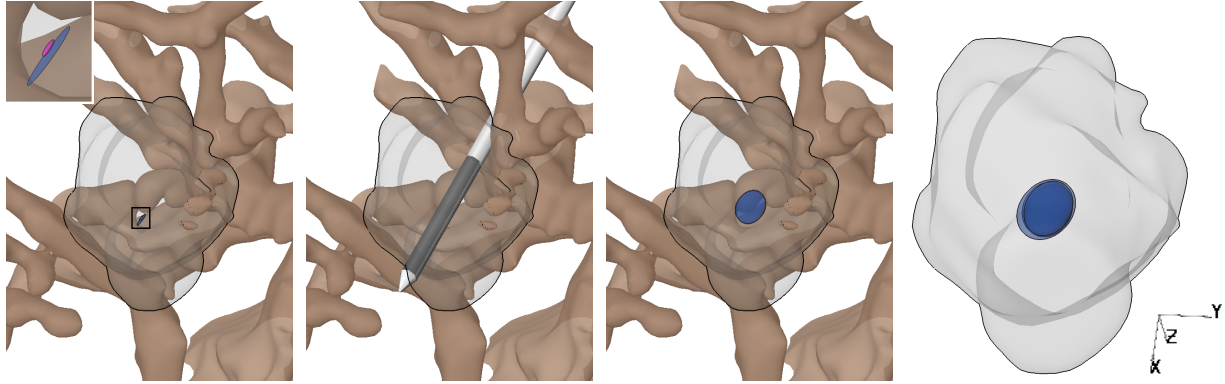
Figure 5: Visualization of the sensitivity of the optimal probe position through an ellipsoidal representation of the covariance matrix. The sensitivity w.r.t. variations in the electric conductivity σ (left, blue ellipsoid) and thermal conductivity λ (left, pink ellipsoid) are shown. In addition, we show the RF probe drawn at the mean of the corresponding placement's distribution for stochastic σ and λ, respectively (middle left). Moreover, the sensitivity w.r.t. a larger variation of σ (i.e., $\sigma \in [0.1, 3.0]^3$ [S/m]) is visualized (middle right) together with a consideration of the corresponding results for the last four refinement levels of the adaptively refined stochastic grid (right). As before, the vascular system D_v (if shown) is displayed in beige-brown and the tumor lesion D_t is displayed in a transparent gray color.

the PDF: large eigenvalues imply that the distribution is wide (has a high variance) in the corresponding direction.

In Fig. 5 we embed the ellipsoid in the surrounding anatomy. Here, we visualize the sensitivity of the model (i.e., of the optimization of only the probe position with fixed orientation) with respect to variations in σ (left, blue ellipsoid) and λ (left, pink ellipsoid) together with the RF probe drawn at the mean of the corresponding placement's distribution for stochastic σ and λ, respectively (middle left). We see that our model (i.e., our optimal probe position) shows no significant sensitivity w.r.t. variations in σ or λ, since the corresponding ellipsoids are very small (see Fig. 5, left) and moreover the mean of the placements distribution for stochastic σ differs from the mean of the placements distribution for stochastic λ by only $0.2 \, \text{mm}$ (see Fig. 5, middle left). Note, that in a second step we also analyzed the sensitivity of the optimal probe position for variations in σ and λ simultaneously, but since we did not obtain a significant sensitivity even for this combined stochasticity, we do not show the corresponding result, here. However, if we enlarge the variations in the electric conductivity $\sigma = (\sigma_n, \sigma_t, \sigma_v)$ to e.g., $[0.1, 3.0]^3$ [S/m] (which is still adequate, since we want to consider uncertainties caused by measurements on animal and/or cadaveric tissue, which further may be afflicted by measurement errors) we see a more significant sensitivity of the optimal probe position (see Fig. 5, middle right). On the right of Fig. 5 we present the result of this sensitivity analysis for different refinement levels of the adaptively refined grid. More precisely, we see the result for level 7, 8, 9 and 10, where i.e., the adaptive refinement level 10 here corresponds to 2576 sampling points in the stochastic space (on a full three dimensional Smolyak grid this would be 6017 sampling points at a resolution of $s = 8$ in terms of polynomial spanning ability). Although the sensitivity analysis for this larger variation of σ did not converge up to the refinement level 10, i.e., the $1 \, \text{mm}$ stopping criterion of our sensitivity analysis (see explanations from above) is not fulfilled, yet, we see that for the last three refinement levels, the ellipsoid does not change significantly.

Finally, we show the sensitivity analysis of the simultaneous optimization of the probe's position and orientation with respect to variations in the electric conductivity σ. Here, again σ varies within the ranges presented at the beginning of Sect. 4. For this combined optimization of both quantities, we see a much larger sensitivity of the optimal probe position (Fig. 7, left and middle) than for the separate optimization of only the probe's position. Since the sensitivity analysis of this combined optimization did not converge up to a refinement level 7, which here corresponds to 2303 sampling points on the adaptively refined grid, we visualized the corresponding ellipsoid for the last three refinement levels 5, 6 and 7. We see, that at least for the last two refinement levels, the ellipsoid does not change significantly any more.
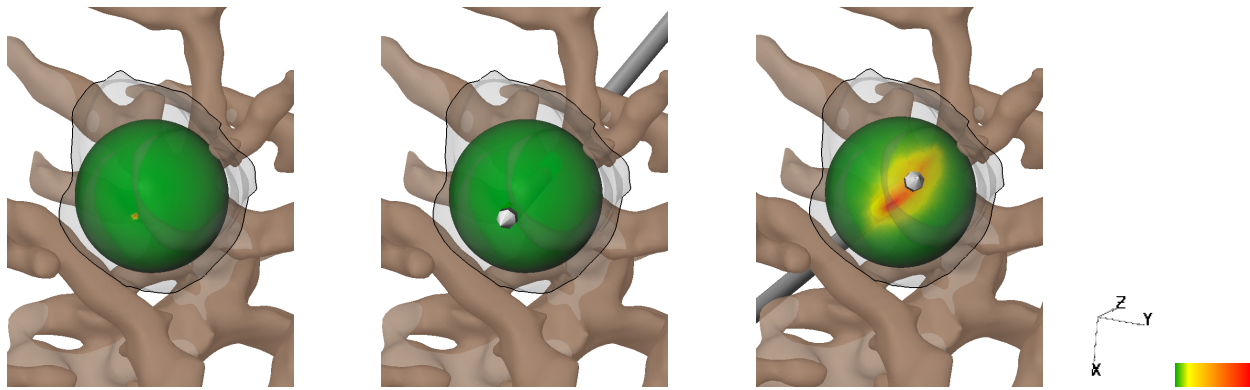
Figure 6: Visualization of the sensitivity (i.e., the PDF) of the optimal probe orientation through a color coding of the sphere. As shown by the color ramp on the right, green colors indicate unlikely orientations, whereas red colors show likely orientations. On the left we see the sensitivity w.r.t. variations in σ within the rather small ranges presented at the beginning of Sect. 4. In the middle we additionally draw the RF probe at the mean of the placement's distribution. On the right we see the sensitivity w.r.t larger variations of σ (i.e., $\sigma \in [0.1, 3.0]^3$ [S/m]) again with the RF probe drawn at the mean of the placement's distribution. As in the previous figures, the vessels D_v are displayed in beige-brown and the tumor D_t is displayed in transparent gray.

4.3 Sensitivity of the Optimal Probe Orientation

The visualization of the PDF of the optimal probe orientation is much easier, since the orientation lies on the two dimensional sphere S^2. In Fig. 6 we show different PDFs of the optimal probe orientation $\bar{a}$ by a color coding of the sphere. More precisely, we show the results of a sensitivity analysis of the optimal probe orientation with fixed probe position for stochastic σ varying within the ranges presented at the beginning of Sect. 4 (Fig. 6, left and middle) and for stochastic $\sigma \in [0.1, 3.0]^3$ [S/m] (Fig. 6, right).

The results confirm our observation from the analysis of the optimal probe location: We have a weak dependence on σ for variations within the rather small ranges presented at the beginning of Sect. 4 and a significant dependence on σ for large variations of this three-dimensional tissue parameter.

Note, that we also analyzed the sensitivity of the optimal probe orientation with fixed position w.r.t. variations in the thermal conductivity λ within the rather small ranges presented at the beginning of Sect. 4. However, since the results do not differ much from the corresponding results for a stochastic electric conductivity σ (i.e., they reveal no significant sensitivity), we do not show them, here.

In (Fig. 7, right) we show the sensitivity of the optimal probe orientation, which we obtained for the combined optimization of the probe's position and orientation described at the end of Section 4.2. As for the optimal probe position, also for the optimal probe orientation we see a much larger sensitivity, when analyzing the combined optimization of both quantities.

We finally conclude that for the combined optimization of the probe's position and orientation and/or for large variations in the electric and/or thermal conductivity the uncertainty of the tissue properties can have a significant influence on the optimal probe placement for RF ablation. The aim of our investigations is to sensitize the final user of a planning software to this uncertainty associated with the results.

5. DISCUSSION AND CONCLUSIONS

We have presented a model for the optimization of the placement of a monopolar probe in radiofrequency ablation that depends on the electric and thermal conductivity of native liver tissue, tumor tissue, and vessels. The deterministic forward model for the simulation of the temperature distribution of the RF ablation, which is used within our optimization, has been extended to a stochastic PDE model with probabilistically distributed material parameters taking
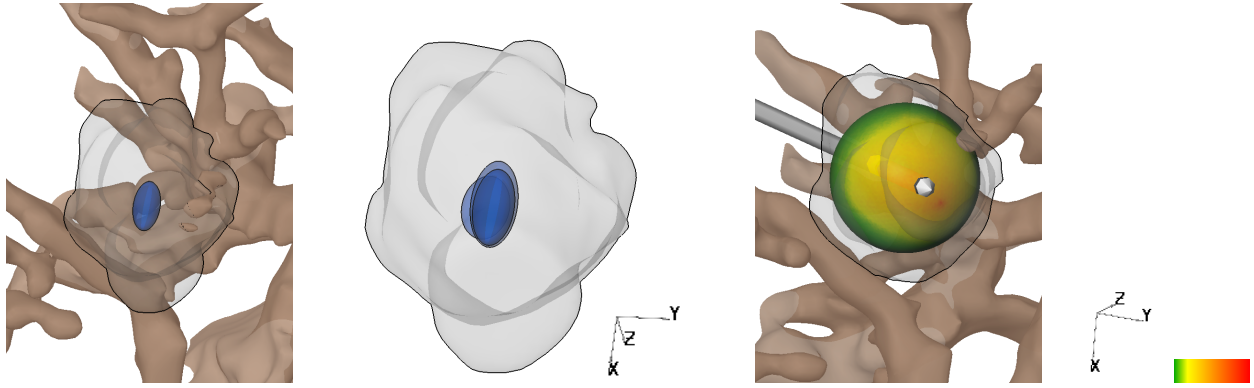
Figure 7: Visualization of the sensitivity of the optimal probe position (left, representation of the covariance matrix via blue ellipsoid) and orientation (right, coloring of the sphere) w.r.t to variations of σ in the ranges described at the beginning of Sect. 4 and obtained for the combined optimization of the probe's position and orientation. In the middle image we see the corresponding sensitivity results for the optimal probe position and for the last three refinement levels of the stochastic grid. Again as in the previous images, the segmented vascular system D_{v} (if shown) is displayed in beige-brown and the segmented lesion D_{t} is displayed transparent gray.

into account the uncertainty associated with electric and thermal conductivities of the tissue. Together with a stochastic finite element method on adaptively refined, hierarchical grids, this approach allows us to evaluate the sensitivity of the optimization results with respect to variations in the material parameters.

We have presented numerical results which are based on a segmented lesion and vascular structures from a real CT scan. Because vector-valued data is optimized (probe location and/or probe orientation) a visualization of the resulting distributions is not straightforward. For the visualization of the distribution of the optimal probe location we presented different approaches. Since a three-dimensional volume rendering of the histograms is difficult to interpret, we use an ellipsoidal representation, which easily reveals the mean and the covariance of the distribution. A visualization of the distribution of the optimal probe orientation is much simpler. Here we showed a color coding of the sphere according to the corresponding PDF.

Our numerical experiments show a significant sensitivity of the temperature profiles w.r.t. variations in the tissue properties. For the optimization however, the separate consideration of only the probe position or only the probe orientation does not show any significant sensitivity for realistic variations in the electric conductivity σ and/or the thermal conductivity λ which are given in the literature for cadaveric animal tissue. However, if we enlarge the variations in order to account for measurement errors and differences between animal and human tissue we see a significant sensitivity even for the optimization of only the probe position or only the probe orientation. If we analyze the combined optimization of the probe's position and orientation, we obtain significant sensitivities, also for the smaller variations of σ.

The optimization of the placement of one monopolar probe presented in this work, easily generalizes to an optimization of the placement of a cluster of probes. Also the study of treatment by bi-polar probes, multi-polar probes, or umbrella-type probes is possible with the framework presented herein. Our investigations in these fields are still in progress. In addition, the approach presented in this paper can be used for many other models in medical simulation including cryosurgery or irreversible electroporation as well. In particular for complicated nonlinear models for which a theoretical sensitivity analysis is cumbersome or even infeasible, our approach is attractive.

With the numerical experiments considered here, we have demonstrated that our approach allows to quantify the robustness of simulation results with respect to the uncertainty involved in the model parameters. In this sense our investigations can sensitize the user (i.e., a radiologist, surgeon, medical doctor) to use simulation results which are based on uncertain parameters with care.

With our investigations we have performed a step toward patient-specific modeling in the field of medical simula-
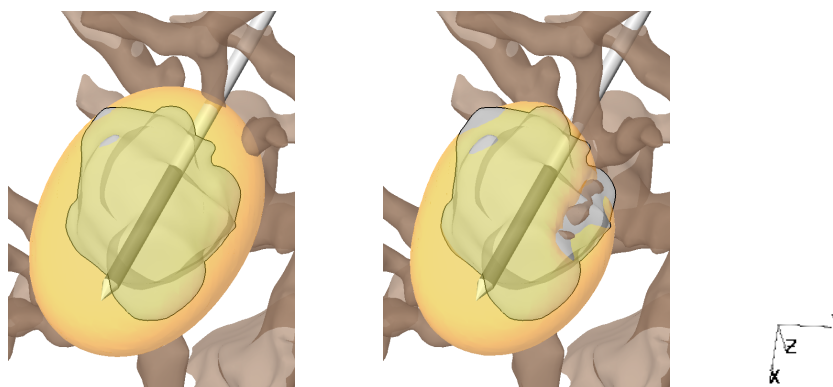
Figure 8: $50\,^\circ$C isosurface of the temperatures calculated with our forward simulation for $\nu_{\text{vessel}} = 0.006067\,\text{s}^{-1}$ (left) and $\nu_{\text{vessel}} = 0.5\,\text{s}^{-1}$ (right). In both calculations the values of σ and λ have been set to the mean values of the intervals presented at the beginning of Sect. 4.

tion – here applied to the optimization of RF ablation. We do not tackle the problem of patient-specific parameters by trying to obtain more accurate material parameters. Instead we consider uncertainty to be an intrinsic attribute of the modeling process.

Our future investigations will involve an optimization of the confidence for the success of the therapy. Moreover, our future investigations will deal with the optimization of the RF ablation under a refined and time-dependent model for the simulation. Thus, we can take into account the nonlinear dependence of the material parameters on the state of the system as well. Also, the consideration of the perfusion coefficients as sources of uncertainty will be a further direction of research. Fig. 8 shows an outlook in this direction. Here, we see the $50\,^\circ$C isosurface of the resulting temperatures of our forward simulation calculated for different values of the relative perfusion rate ν_{vessel} (see Sect. 2.1), i.e., for $\nu_{\text{vessel}} = 0.006067\,\text{s}^{-1}$ (capillary perfusion) and for $\nu_{\text{vessel}} = 0.5\,\text{s}^{-1}$ (strong perfusion for which the temperature within the vascular system approximately remains body temperature). All other tissue parameters (i.e., the conductivity values) have been set to the mean values of the intervals presented at the beginning of Sect. 4. We see, that we get a significant difference in the shape of the corresponding temperature profiles, which motivates a deeper analysis of uncertain perfusion coefficients.

ACKNOWLEDGMENT

REFERENCES

1. Baegert, C., Villard, C., Schreck, P., Soler, L., and Gangi, A., Trajectory optimization for the planning of percutaneous radiofrequency ablation of hepatic tumors, *Comput. Aided Surg.*, 12(2):82–90, 2007.

2. Kim, Y. S., Rhim, H., Cho, O. K., Koh, B. H., and Kim, Y., Intrahepatic recurrence after percutaneous radiofrequency ablation of hepatocellular carcinoma: analysis of the pattern and risk factors, *Eur. J. Radiol.*, 59(3):432–441, 2006.

3. Stein, T., *Untersuchungen zur Dosimetrie der hochfrequenzstrominduzierten interstitiellen Thermotherapie in bipolarer Technik*, Vol. 22 of Fortschritte in der Lasermedizin, Müller and Berlien, 2000.

4. Deuflhard, P., Weiser, M., and Seebaß, M., A new nonlinear elliptic multilevel FEM applied to regional hyperthermia, *Comput. Vis. Sci.*, 3(3):115–120, 2000.

5. Jain, M. K. and Wolf, P. D., A three-dimensional finite element model of radiofrequency ablation with blood flow and its experimental validation, *Ann. Biomed. Eng.*, 28(9):1075–84, 2000.

6. Tungjitkusolmun, S., Staelin, S. T., Haemmerich, D., Tsai, J.-Z., Cao, H., Webster, J. G., Lee, F. T., Mahvi, D. M., and Vorperian, V. R., Three-dimensional finite-element analyses for radio-frequency hepatic tumor ablation, *IEEE Trans. Biomed. Eng.*, 49(1):3–9, 2002.

7. Harth, O., Wasserhaushalt, Stoff und Flüssigkeitstransport, In: Schmidt, R. F. and Thews, G. (Eds.), *Physiologie des Menschen*. Springer, 1993.

8. Bowman, H. F., Heat transfer and thermal dosimetry, *J. Microwave power*, 16(2), 1981.

9. Altrogge, I., Kröger, T., Preusser, T., Büskens, C., Pereira, P. L., Schmidt, D., Weihusen, A., and Peitgen, H.-O., Towards optimization of probe placement for radio-frequency ablation, *LNCS*, 4190:486–493, 2006.

10. Altrogge, I., Preusser, T., Kröger, T., Büskens, C., Pereira, P. L., Schmidt, D., and Peitgen, H.-O., Multi-scale optimization of the probe placement for radio-frequency ablation, *Academic Radiology*, 14(11):1310–1324, 2007.

11. Haase, S., Ring, W., Altrogge, I., Kröger, T., and Preusser, T., Optimization of probe placement for radio-frequency ablation using shape derivatives, *in preparation*, 2011.

12. Altrogge, I., Optimization of the probe placement for radiofrequency ablation, PhD thesis, University of Bremen, 2009.

13. Xiu, D. and Shen, J., Efficient stochastic galerkin methods for random diffusion equations, *Journal of Computational Physics*, 228:266–291, 2009.

14. Welp, C., Siebers, S., Ermert, H., and Werner, J., Investigation of the influence of blood flow rate on large vessel cooling in hepatic radiofrequency ablation, *Biomed. Tech.*, 51:337–346, 2006.

15. Roggan, A., *Dosimetrie thermischer Laseranwendungen in der Medizin*, Vol. 16 of Fortschritte in der Lasermedizin, Müller and Berlien, 1997.

16. Preusser, T., Weihusen, A., and Peitgen, H.-O., On the modelling of perfusion in the simulation of RF-ablation, In *Proc. SimVis*, Magdeburg, 2005.

17. Villard, C., Soler, L., and Gangi, A., Radiofrequency ablation of hepatic tumors: simulation, planning, and contribution of virtual reality and haptics, *Comp. Meth. Biomech. & Biomed. Eng.*, 8(4):215–227, August 2005.

18. Butz, T., Warfield, S. K., Tuncali, K., Silverman, S. G., Sonnenberg, E.v., Jolesz, F. A., and Kikinis, R., Pre- and intra-operative planning and simulation of percutaneous tumor ablation, *LNCS*, 1935:395–416, 2000.

19. Khalil-Bustany, I. S., Diederich, C. J., Polak, E., and Kirjner-Neto, C., Minmax optimization-based inverse treatment planning for interstitial thermal therapy, *Int. J. Hyperthermia*, 14(4):347–366, 1998.

20. Seitel, A., Engel, M., Sommer, C. M., Radeleff, B. A., Essert-Villard, C., Baegert, C., Fangerau, M., Fritzsche, K. H., Yung, K., Meinzer, H. P., and Maier-Hein, L., Computer-assisted trajectory planning for percutaneous needle insertions, *Med. Phys.*, 38(6):3246–3259, 2011.

21. Villard, C., Baegert, C., Schreck, P., Soler, L., and Gangi, A., Optimal trajectories computation within regions of interest for hepatic rfa planning, *LNCS*, 3750:49–56, 2005.

22. Kapoor, A., Li, M., and Wood, B., Mixed variable optimization for radio frequency ablation planning, *Medical Imaging 2011: Visualization, Image-Guided Procedures, and Modeling*, 7964, March 2011.

23. Chen, C.-C. R., Miga, M. I., and Jr, R. L. G., Optimizing electrode placement using finite-element models in radiofrequency ablation treatment planning, *IEEE Trans. Biomed. Eng.*, 56(2):237–245, 2009.

24. Wiener, N., The homogeneous chaos, *American Journal of Mathematics*, 60(4):897–936, 1938.

25. Meecham, W. C. and Jeng, D. T., Use of Wiener-Hermite expansion for nearly normal turbulence, *J. Fluid Mech.*, 32:225–249, 1968.

26. Chorin, A. J., Hermite expansions in Monte Carlo computation, *J. Comput. Phys.*, 8:471–482, 1971.

27. Chorin, A. J., Gaussian fields and random flow, *J. Fluid Mech.*, 63:21–32, 1974.

28. Maltz, F. H. and Hitzl, D. L., Variance reduction in Monte Carlo computations using multi-dimensional Hermite polynomials, *J. Comput. Phys.*, 32:345–376, 1979.

29. Deb, M. K., Babuška, I. M., and Oden, J. T., Solutions of stochastic partial differential equations using Galerkin finite element techniques, *Comput. Methods Appl. Mech. Eng.*, 190:6359–6372, 2001.

30. Maître, O. P. L., Reagan, M. T., Najm, H. N., Ghanem, R. G., and Knio, O. M., A stochastic projection method for fluid flow II.: random process, *Journal of Computational Physics*, 181(1):9–44, 2002.

31. Xiu, D. B. and Karniadakis, G. E., Modeling uncertainty in steady state diffusion problems via generalized polynomial chaos, *Comput. Methods Appl. Mech. Eng.*, 191:4927–4948, 2002.

32. Xiu, D. B. and Karniadakis, G. E., Modeling uncertainty in flow simulations via generalized polynomial chaos, *J. Comput. Phys.*, 187:137–167, 2003.

33. Geneser, S. E., Kirby, R. M., and MacLeod, R. S., Application of stochastic finite element methods to study the sensitivity of ecg forward modeling to organ conductivity, *IEEE Transactions on Biomedical Engineering*, In Press, 2007.

34. Xiu, D. and Hesthaven, J. S., High-order collocation methods for differential equations with random inputs, *SIAM J. Sci. Comput.*, 27(3):1118–1139, 2005.

35. Eiermann, M., Ernst, O. G., and Ullmann, E., Computational aspects of the stochastic finite element method, *Comput. Visual. Sci.*, 10(1):3–15, 2007.

36. Babuška, I., Tempone, R., and Zouraris, G. E., Solving elliptic boundary value problems with uncertain coefficients by the finite element method: the stochastic formulation., *SIAM J. Numer. Anal.*, 42(2):800–825, 2004.

37. Wan, X. and Karniadakis, G. E., Multi-element generalized polynomial chaos for arbitrary probability measures, *SIAM Journal of Scientific Computing*, 28:901–928, 2006.

38. Foo, J. and Karniadakis, G. E., Multi-element probabilistic collocation method in high dimensions, *Journal of Computational Physics*, 229:1536–1557, 2010.

39. Fletcher, R., *Practical Methods of Optimization*, John Wiley & Sons, 2000.

40. Wang, J. and Zabaras, N., Hierarchical Bayesian models for inverse problems in heat conduction, *Inverse Problems*, 21:183–206, 2005.

41. Wang, J. and Zabaras, N., Using Bayesian statistics in the estimation of heat source in radiation, *Int. J. Heat and Mass Transfer*, 48:15–29, 2005.

42. Wang, J. and Zabaras, N., A Markos random field model to conatmination source identification in porous media flow, *Int. J. Heat and Mass Transfer*, 49:939–950, 2006.

43. Badrinarayanan, V. A. and Zabaras, N., Stochastic inverse heat conduction using a spectral approach, *International Journal for Numerical Methods in Engineering*, 60:1569–1593, 2004.

44. Tiesler, H., Kirby, R. M., Xiu, D., and Preusser, T., Stochastic collocation for optimal control problems with stochastic pde constraints, *SIAM Journal on Optimization*, Under Review, 2011.

45. Bourquain, H., Schenk, A., Link, F., Preim, B., Prause, G., and Peitgen, H.-O., Hepavision2: A software assistant for preoperative planning in living-related liver transplantation and oncologic liver surgery., *CARS*, pp. 341–346, 2002.

46. Haemmerich, D., Chachati, L., Wright, A. S., Mahvi, D. M., Lee Jr, F. T., and Webster, J. G., Hepatic radiofrequency ablation with internally cooled probes: effect of coolant temperature on lesion size., *IEEE Trans. Biomed. Eng.*, 50(4):493–500, 2003.

47. Kröger, T., Altrogge, I., Preusser, T., Pereira, P. L., Schmidt, D., Weihusen, A., and Peitgen, H.-O., Numerical simulation of radio frequency ablation with state dependent material parameters in three space dimensions,

LNCS, 4191:380–388, 2006.

48. Pennes, H. H., Analysis of tissue and arterial blood temperatures in a resting forearm, *J. Appl. Physiol.*, 1:93–122, 1948.

49. Jain, R. K., Grantham, F. H., and Gullino, P. M., Blood flow and heat transfer in Walker 256 mammary carcinoma, *J. Natl. Caner Inst.*, 69:927–931, 1979.

50. Creeze, J. and Lagendijk, J. J. W., Temperature uniformity during hyperthermia: the impact of large vessels, *Phys. Med. Biol.*, 37(6):1321–1337, 1992.

51. Lagendijk, J. J. W., The influence of bloodflow in large vessels on the temperature distribution in hyperthermia, *Phys. Med. Biol.*, 27(1):17–23, 1982.

52. Creeze, J., Mooibroek, J., Lagendijk, J. J. W., and van Leeuwen, G. M. J., The theoretical and experimental evaluation of the heat balance in perfused tissue, *Phys. Med. Biol.*, 39:813–832, 1994.

53. Welp, C., Investigation of the influence of blood flow rate on large vessel cooling in hepatic radiofrequency ablation, *Biomed. Tech. (Berl.)*, 51(5-6):337–346, 2006.

54. Sheu, T. W. H., Chou, C. W., Tsai, S. F., and Liang, P. C., Three-dimensional analysis for radio-frequency ablation of liver tumor with blood perfusion effect, *ComputerMethodsinBiomechanicsandBiomedical Engineering*, 8(4):229–240, 2005.

55. Arrhenius, S., Über die Reaktionsgeschwindigkeit bei der Inversion von Roherzucker durch Säuren, *Z. Phys. Chem.*, 4:226–248, 1887.

56. Preusser, T., Liehr, F., Rumpf, M., Sauter, S., Weikard, U., and Peitgen, H.-O., Simulation of radio-frequency ablation using composite finite element methods, In *Perspective in Image Guided Surgery*, pp. 303–310, Remangen, 2004.

57. Liehr, F., Preusser, T., Rumpf, M., Sauter, S., and Schwen, L. O., Composite finite elements for 3D image based computing, *Computing and Visualization in Science*, 12(4):171–188, April 2009.

58. Pätz, T., Kröger, T., and Preusser, T., Simulation of radiofrequency ablation including water evaporation, In *IFMBE Proceedings*, Vol. 25(4), pp. 1287–1290. Springer, 2009.

59. Hackbusch, W., *Multi-Grid Methods and Applications*, Vol. 4 of Springer Series in Computational Mathematics, Springer, 1985.

60. Xiu, D., *Numerical methods for stochastic computations*, Princeton Univeristy Press, Princeton, New Jersey, 2010.

61. Ghanem, R. G. and Spanos, P., *Stochastic Finite Elements: A Spectral Approach*, Springer-Verlag, New York, NY, 1991.

62. Xiu, D. B. and Karniadakis, G. E., The Wiener-Askey polynomial chaos for stochastic differential equations, *SIAM J. Sci. Comput.*, 24:619–644, 2002.

63. Xiu, D. B. and Hesthaven, J. S., High-order collocation methods for differential equations with random inputs, *SIAM Journal on Scientific Computing*, 27(3):1118–1139, 2005.

64. Keese, A., Numerical solution of systems with stochastic uncertainties : A general purpose framework for stochastic finite elements, PhD thesis, Technical University Braunschweig, 2004.

65. Kröger, T., Altrogge, I., Konrad, O., Kirby, R. M., and Preusser, T., Estimation of probability density functions for parameters sensitivity analyses, In *Proc. SimVis*, pp. 61–74, Magdeburg, 2008.

66. Kaipio, J. and Somersalo, E., Statistical inverse problems: Discretization, model reduction and inverse crimes", *Journal of Computational and Applied Mathematics*, 1098:493–504, 2007.